

Catalysis Science & Technology

Sulfur Substitution in Fe-MOF-74: Implications for Electrocatalytic CO₂ and CO Reduction from an *ab initio* Perspective

Journal:	Catalysis Science & Technology
Manuscript ID	CY-ART-02-2024-000217.R1
Article Type:	Paper
Date Submitted by the Author:	19-Mar-2024
Complete List of Authors:	McCarver, Gavin; NIST Center for Neutron Research, Yildirim, Taner; NIST, NIST Center for Neutron Research Zhou, Wei; NIST, NIST Center for Neutron Research

SCHOLARONE™ Manuscripts

Journal Name

ARTICLE TYPE

Cite this: DOI: 00.0000/xxxxxxxxxx

Sulfur Substitution in Fe-MOF-74: Implications for Electrocatalytic CO_2 and CO Reduction from an *ab initio* Perspective[†]

Gavin A. McCarver*, Taner Yildirim, Wei Zhou

Received Date Accepted Date

DOI: 00.0000/xxxxxxxxxx

Employing first-principles methods, we investigated the electrocatalytic reduction of CO2 and CO on two Fe-based MOFs: Fe₂DOBDC and Fe₂DSBDC. Our primary objective was to discern the impact of substituting S atoms into the framework while maintaining the topological structure. We anticipated significant changes in reduction reactions due to differences in chemical properties such as electronegativity, atomic radius, polarizability, and charge density upon replacing O atoms with S atoms. Atomic charge analysis highlights some of these differences by showing the equatorial Fe-O/S bonds of Fe₂DSBDC are less polarized and result in smaller positive and negative charges on the Fe and O/S atoms, respectively. Additionally, the larger S atoms are expected to weaken adsorbate binding due to less favorable van der Waals interactions near the open-metal Fe site. Consequently, the less electropositive Fe site and the larger S atoms of Fe₂DSBDC impede the adsorption of reduced CO₂ and CO products, while the more electropositive Fe site and smaller O atoms of Fe₂DOBDC strongly favor product adsorption. Specifically, the weak binding of HCOOH and CH₂O intermediates on Fe₂DOBDC (ΔG of -0.07 eV and -0.11 eV, respectively) indicates feasible further reduction to CH₂O and CH₄ for CO₂RR and CORR, respectively. Conversely, these adsorbates exhibit unfavorable binding to the Fe site of Fe₂DSBDC (ΔG of +0.14 eV and +0.25 eV, respectively), limiting further reduction possibilities. Thus, CO₂ and CO reduction on Fe₂DSBDC are likely to yield only 2e⁻ products (HCOOH and CH₂O, respectively), whereas Fe₂DOBDC is expected to produce deeper reduction products (CH₂O and CH₄, respectively). Additionally, significant differences in free energy for the first reduction steps post-sulfur substitution indicate more favorable energetics for both CO2 and CO reductions ($\Delta G = -0.12$ eV and -0.58 eV, respectively). These findings lay the groundwork for designing novel MOFs with tunable reaction behaviors by strategically replacing O atoms with heavier S atoms in the MOF scaffold.

1 Introduction

The conversion of carbon dioxide (CO₂) and carbon monoxide (CO) into higher-value fuels, feedstock materials, and fine chemicals stands at the forefront of exten-

sive research endeavors, offering a promising approach to diminish our dependence on fossil fuels. $^{1-3}$ Electrocatalysis, a versatile process adept at reducing both ${\rm CO_2}^{4,5}$ and ${\rm CO}^{5,6}$ has emerged as a vital technique for converting these molecules into more value-added materials. Within this landscape, metal-organic frameworks (MOFs), a burgeoning class of materials, exhibit significant potential for electrocatalytic reduction reactions. 7 These coordination polymers, featuring metal nodes coordinated to organic linkers, boast uniform and well-characterized active sites akin to traditional homogeneous catalysts while maintain-

National Institute of Standards and Technology, Center for Neutron Research, Gaithersburg, Maryland 20899-6102, United States; E-mail: gavin.mccarver@nist.gov

† Electronic Supplementary Information (ESI) available: reaction energetics and Cartesian coordinates for each reactant, intermediate, and product. See DOI: 00.0000/00000000.

Journal Name, [year], $[yol_{|}]_1$

Fig. 1 Molecular structures of the DOBDC (left) and DSBDC (right) ligands used to construct the $\rm Fe_2DOBDC$ and $\rm Fe_2DSBDC$ MOFs, respectively.

ing a heterogeneous structure, effectively bridging the catalytic realms.⁸

Identifying and synthesizing MOFs with potential as electrocatalysts for reduction reactions presents a considerable challenge, demanding materials with intrinsic charge-carrying capabilities to facilitate essential electron transfer during reduction processes. 9,10 To illustrate, Sun and colleagues demonstrated a notable breakthrough in enhancing the electrical conductivity of Fe-MOF-74 (Fe₂DOBDC, DOBDC = 2,5-dihydroxybenzene-1,4-dicarboxylate, Figure 1). 11 They achieved this by introducing thiophenoxide groups through the replacement of phenoxide groups, utilizing 2,5-disulfhydrybenzene-1,4-dicarboxylate (DSBDC). Crucially, this modification resulted in an increased electrical conductivity without altering the well-established MOF-74 topology, now featuring (-Fe-S-)_∞ chains. The significant improvement in electrical properties was attributed to the presence of the heavier chalcogenide atoms. This aligns with the historical chemistry of organic conductors, where such elements typically contribute to enhancements in electrical conductivity ¹². Additionally, recent work by Ali et al. have shown the utility of sulfur substitution in MOFs to modify the CO₂ reduction reaction. ^{13,14}

In light of the enhanced electrical conductivity observed in Fe₂DSBDC, we aimed to expand upon our earlier theoretical exploration focused on X-MOF-74 (X = Mg, Mn, Fe, Co, Ni, Cu, Zn) for the reduction of CO₂. ¹⁵ Our previous work addressed the unexplored realm of CO₂ reduction on Fe-MOF-74, a system that has not been previously studied either experimentally or computationally for this specific purpose. In this investigation, Fe-MOF-74 demonstrated substantial promise for CO₂ reduction, showcasing strong binding of reduced intermediates to limit desorption and push the reduction completely towards methane (CH₄) formation, a low limiting potential (0.32 eV), and a favorable selectivity for CO₂ reduction over hydrogen reduction. Given that both the Fe₂DOBDC and Fe₂DSBDC materials share an identical topological structure, delving

into how the introduction of heavier chalcogenide atoms might influence the reduction of both ${\rm CO}_2$ and ${\rm CO}$ became imperative.

The introduction of S atoms in DSBDC brings about several distinct properties that can significantly influence catalytic reactivity for these reduction reactions. Firstly, the lower electronegativity of S atoms (2.659) compared to O atoms (3.758) 16 results in a less pronounced bond polarity between Fe and S atoms. Additionally, the larger, softer S atoms possess lower charge density and higher polarizability than the harder O atoms, contributing to distinct chemical interactions. 17 Furthermore, the larger S atoms might induce increased repulsive van der Waals interactions between the Fe site and adsorbate molecules. ¹⁸ Lastly, differing orbital interactions between Fe and O versus Fe and S atoms contribute to a larger band gap of 1.92 eV in Fe₂DSBDC compared to the 1.47 eV band gap in Fe₂DOBDC, potentially leading to notable differences for reduction reactions. 11 This presents an opportunity to finely adjust these reactions based solely on the presence or absence of the heavier S atoms, adding a layer of versatility of these promising materials.

Given the well-known reactivity of Fe centers in Fe₂DOBDC, ¹⁹ electrochemical reduction reactions might present experimental challenges. Moreover, the stability of many MOFs in solvated conditions is a crucial consideration. Therefore, it is imperative to ensure the stability of both Fe₂DOBDC and Fe₂DSBDC materials under solvated and electrochemical conditions. Previous studies by Van Phuc et al. 20 and Choi et al. 21 have thoroughly examined the stability and applicability of X-MOF-74 materials (where X = Co, Ni, Cu, Zn) under electrochemical conditions using 0.1 - 0.5 M KHCO3 as the electrolyte. Furthermore, there is abundant literature evidence of Febased catalysts being employed for CO2 reduction reactions under DMF, the same solvent used during the synthesis of Fe₂DOBDC and Fe₂DSBDC by Sun et al. ¹¹ Hence, these studies collectively suggest that the Fe₂DOBDC and Fe₂DSBDC materials should demonstrate stability under electrochemical conditions and DMF solvation.

Our results highlight distinctive chemical behaviors arising from the Fe-O and Fe-S bonds in Fe₂DOBDC and Fe₂DSBDC, respectively, underscoring the significant variations in their responses to closed-shell products from CO₂ and CO reduction. We also study the reduction of hydrogen on these materials as this reaction often competes with other reduction reactions in acidic solutions. The Fe₂DOBDC MOF exhibits heightened affinity for reduced CO₂ and CO intermediates, fostering the formation of more deeply reduced products, including CH₂O

Reaction	E ⁰ / [V vs RHE]
$CO_2 + 2H^+ + 2e^- \rightarrow HCOOH$	-0.61
$CO_2 + 2H^+ + 2e^- \rightarrow CO + H_2O$	-0.53
$CO_2 + 4H^+ + 4e^- \rightarrow CH_2O + H_2O$	-0.48
$CO + 6H^{+} + 6e^{-} \rightarrow CH_{4} + H_{2}O$	0.26

Table 1 Electrochemical reactions with equilibrium potentials.

(formaldehyde) and CH₄. In contrast, the Fe₂DSBDC MOF results in weakened interactions with closed-shell reactants, intermediates, and end products. We attribute this behavior to the larger size of the S atoms resulting in less favorable interactions and the less polarized equatorial Fe-O/S bonds which result in a less electropositive Fe site. Consequently, Fe₂DSBDC predominately yields 2e⁻ reduced products, specifically HCOOH (formic acid) and CH2O, following CO2 and CO reduction, respectively (see Table 1 for equilibrium potentials). ²² Notably, the limiting potential for CO2 reduction remains consistent across the various ligand backbones, while CO reduction exhibits significant changes in limiting potential. These outcomes underscore the substantial influence of the ligand's identity within the MOF scaffold, shaping the products emerging from CO2 and CO reduction, and highlighting the pivotal role of metal-ligand binding disparities. This study not only sheds light on the distinctive metal-ligand binding interactions in Fe₂DOBDC and Fe₂DSBDC but also provides a framework for the strategic engineering of other MOFs, aiming to uncover novel metal-ligand interactions that could impart significant variations in reactivities for diverse reduction reactions.

2 Computational Details

In the investigation of the Fe₂DOBDC and Fe₂DSBDC materials, we use two cluster models to investigate the CO_2 and CO reduction reactions at the open metal sites (OMS). Our justification for using cluster models instead of fully periodic systems lies in the extensive prior literature examining MOF-74 in particular and MOFs in general for different applications. ²³ Our chosen cluster model for MOF-74 follows previous work conducted by Verma and colleagues. ²⁴ Each MOF was represented by an 88-atom section, comprising three Fe sites and six DEBDC (E = O, S) ligands. Dangling valencies were appropriately capped to maintain a neutral charge. Additionally, each Fe site was coordinated with a DMF ligand, effectively simulating the first solvation shell. Figure 2 shows representations of the models for Fe₂DOBDC and Fe₂DSBDC, respectively.

Our computational protocol follows our prior research on the utilization of cluster models of MOFs for catalytic reduction reactions. ^{15,25} We employed the M06L²⁶ den-

sity functional with D3zero dispersion corrections²⁷, as implemented in ORCA version 5.0.3.28 Standard SCF and optimization criteria were maintained, and unrestricted Kohn-Sham wavefunctions were assumed for all calculations. The central Fe atom was assigned using the def2-TZVPP basis set, the first coordination sphere around the central Fe atom and adsorbate atoms were assigned the def2-TZVP basis set, and all other atoms were assigned the def2-SV(P) basis set.²⁹ Furthermore, we employed the resolution of identity (RI) 30 method to accelerate the computation of four-index integrals using the def2/J auxiliary basis set. 31 Implicit solvent effects were included via the conductor-like polarizable continuum model (CPCM), utilizing DMF as the solvent. 32 Charge model 5 (CM5) atomic charges³³ and other properties are calculated using the Multiwfn program.³⁴ Orbital localization is performed using the Pipek-Mezey method³⁵ and visualized with Iboview. 36,37

The free energy (G) of each reactant, intermediate, and product is the basis for our energy calculations, and is determined according to:

$$G = E + I + H - TS - eU \tag{1}$$

Here, *E* represents the total electronic energy, *I* comprises the total internal energy, including zero-point and thermal energies, and *H* and *S* denote the enthalpy and entropy,

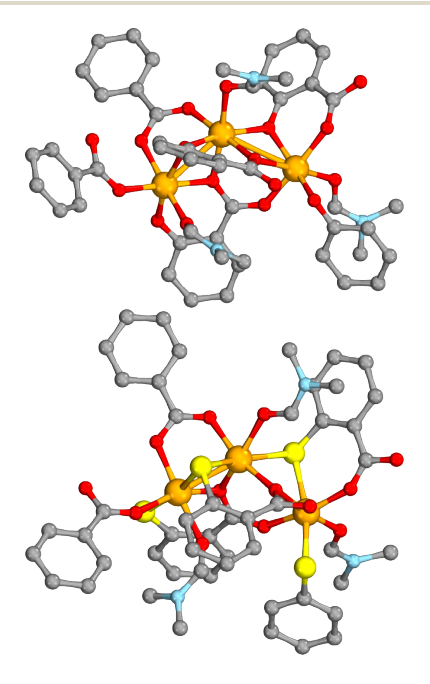


Fig. 2 Cluster models for the Fe₂DOBDC (top) and Fe₂DSBDC (bottom) MOFs. Hydrogen atoms removed for clarity. Color code: C (grey), N (blue), O (red), S (yellow), Fe (orange).

respectively, calculated at a temperature (T) of 298.15 K. These values are calculated following an analytical frequency calculation using the quasi-rigid rotor harmonic oscillator (Qausi-RRHO) approximation. 38 Lastly, eU is the effect of an applied potential U for each elementary step (e). We assumed that each reduction step proceeds through a proton-coupled electron transfer (PCET) mechanism as an initial approximation. 39,40 Essentially, this involves the addition of a hydrogen atom as a H⁺/e⁻ pair in each elementary step of the reaction. The reaction energy of each step of the reduction reaction are referenced relative to the energy of the MOF cluster, a CO2 molecule, and a varying number of H⁺/e⁻ pairs, depending on the number of PCET steps that have occurred. We considered the energy of a single H⁺/e⁻ pair as 1/2 the energy of an H₂ molecule, following the computational hydrogen electrode (CHE) model. 41 The limiting potential for each closed-shell product is determined as the highest free energy difference (ΔG_{max}) between two elementary steps of the reaction.

3 Results & Discussion

3.1 Electronic Structure of Fe₂DOBDC and Fe₂DSBDC Clusters

Electronic structure disparities between the Fe₂DOBDC and Fe₂DSBDC clusters are evident across various properties, notably the atomic charges of the Fe atoms. Significant differences emerge, with values of 0.63 and 0.48 for Fe₂DOBDC and Fe₂DSBDC, respectively (Table 2). The introduction of the heavier chalcogenides results in a more diminished positive charge on the Fe center, counteracted by less negatively charged equatorial atoms (both O and S). In Fe₂DOBDC, the average atomic charge for the four equatorial O atoms is -0.35, while in Fe₂DSBDC, the equatorial O and S atoms show an average atomic charge of -0.27. These distinctions between the Fe centers and the equatorial atoms suggest a higher bond polarity in the Fe₂DOBDC cluster compared to Fe₂DSBDC. This contrast becomes more pronounced following reduction through the addition of an electron to the cluster. The charge of the Fe centers undergoes minimal change (to 0.57 and 0.45 for Fe₂DOBDC and Fe₂DSBDC, respectively), indicating the unlikelihood of the additional electron residing on the Fe centers. In contrast, the equatorial O atoms of Fe₂DOBDC become more negatively charged by an average of -0.10, while the O and S equatorial atoms of Fe₂DSBDC exhibit a smaller change of -0.05. These trends imply that the Fe₂DSBDC material should demonstrate enhanced electrical conductivity due to the greater electron delocalization within the cluster, aligning with the findings of Sun et al.. 11

In both Fe₂DOBDC and Fe₂DSBDC clusters, each Fe center is presumed to adopt a high-spin, S=2 quintet spin configuration, as established in prior studies.²⁴ This configuration gives rise to a single β electron in the d-orbitals of each Fe center, a characteristic attributed by Sun et to the high electrical conductivity of these materials. The molecular orbitals where these β electrons reside exhibit considerable overlap among the Fe centers for the Fe₂DSBDC cluster while little overlap is observed for the Fe₂DOBDC cluster (Figure S1). This heightened orbital overlap, in conjunction with the (-Fe-S-)_∞ chains, likely contributes to the superior electrical conductivity observed in the Fe₂DSBDC material. Anticipated variations in the reduction reactions' performance between the two materials stem from these electronic structure differences.

The initial step of the reduction reactions involves activation through solvent removal. On neutral clusters, this process is unfavorable, with ΔG values of 0.39 eV and 0.14 eV for Fe₂DOBDC and Fe₂DSBDC, respectively. However, upon reduction, the removal of the DMF adsorbate becomes slightly favorable ($\Delta G = -0.09$ eV) on the Fe₂DOBDC cluster and more favorable ($\Delta G = -0.25$ eV) on the Fe₂DSBDC cluster. For simplicity, we will describe each elementary step of the reduction reaction, assuming a PCET mechanism, as quantifying the free energy of a proton using DFT is challenging. However, we will discuss the activation of CO₂ on the singly reduced clusters to evaluate the activation barrier (as discussed below).

3.2 Hydrogen Evolution Reaction (HER)

As hydrogen reduction often competes with other reduction reactions in acidic solutions, it is essential to explore on any new catalyst to assess the interplay between these processes. Due to the softer nature of sulfur atoms within Fe₂DSBDC, we conducted tests on hydrogen adsorption at these sites. However, we observed that adsorption was less favorable on the sulfur sites compared to the Fe site by 0.12 eV. The formation of *H species at the Fe sites of Fe₂DOBDC and Fe₂DSBDC clusters results in nearly identical formation energies of 1.30 eV and 1.31 eV, respectively (as illustrated in Figures S2-S3). Here, the * symbol indicates surface adsorption of the intermediate. Similarly, the Fe-H bond lengths are consistent at 1.54 Å in both clusters, and the localized MOs composed of the Fe-H bond exhibit orbital energies of -0.25 eV (refer to Figure S4). A slight decrease in the atomic charge of the Fe centers of approximately -0.10 is observed following the formation of the Fe-H intermediates, while the hydro-

Table 2 CM5 atomic charges of the neutral and singly-reduced Fe $_2$ DOBDC and Fe $_2$ DSBDC clusters a

	Fe ₂ DOBDC	[Fe ₂ DOBDC] Fe ₂ DSBDC [Fe ₂ DSB]		[Fe ₂ DSBDC]
Fe	0.63	0.57	0.48	0.45
O_{ax}	-0.36	-0.35	-0.36	-0.36
O_{eq}/S_{eq}	-0.35	-0.45	-0.27	-0.32
O_{DMF}	-0.34	-0.33	-0.33	-0.32

 $^{^{\}rm a}$ $O_{\rm ax}$ denotes the axial O atom, $O_{\rm eq}/S_{\rm eq}$ represents the average atomic charges of the O and/or S equatorial atoms, and $O_{\rm DMF}$ pertains to the O atom of the adsorbed DMF molecule.

Table 3 CM5 atomic charges (q), inter-atomic distances (R, Å), and bond angles (A, $^{\circ}$) for CO₂ activation^a

		Fe ₂ DOBDC			Fe ₂ DSBDC		
	CO ₂	*CO ₂	*CO ₂ ‡	*OCO	*CO ₂	*CO ₂ ‡	*OCO
q_{O^1}	-0.21	-0.19	-0.26	-0.38	-0.21	-0.27	-0.33
q_{C}	0.43	0.42	0.32	0.10	0.40	0.27	0.14
q_{O^2}	-0.21	-0.21	-0.24	-0.39	-0.21	-0.29	-0.37
Σq_{CO_2}	0.01	0.02	-0.18	-0.67	0.02	-0.29	-0.56
R _{Fe-O¹}		2.684	2.548	2.802	4.171	3.212	2.971
$R_{\text{Fe-C}}$		3.147	2.529	2.051	3.919	2.516	2.069
R_{Fe-O^2}		3.933	3.311	2.697	4.037	2.802	2.448
R_{C-O^1}	1.159	1.163	1.187	1.228	1.160	1.185	1.211
R_{C-O^2}	1.159	1.157	1.176	1.231	1.160	1.194	1.232
$A_{O^1-C-O^2}$	180.0	178.1	160.1	137.0	178.1	153.4	139.9

 $^{^{\}rm a}$ *OCO refers to the fully activated CO $_{\rm 2}$ complex. O $^{\rm 1}$ and O $^{\rm 2}$ refer to the O atoms furthest from and closest to the Fe site, respectively.

gen atoms remain slightly negatively charged at -0.12 for both clusters. Furthermore, the $\rm H_2$ molecule formed following a second PCET step shows weak physisorption to the Fe centers, with binding energies of 0.11 eV and 0.00 eV for Fe₂DOBDC and Fe₂DSBDC, respectively. Consequently, despite significant electronic structure differences between the Fe₂DOBDC and Fe₂DSBDC clusters, the reduction of hydrogen is anticipated to follow nearly identical energetics with limiting potentials of approximately 1.30 eV.

3.3 CO₂ Reduction Reaction (CO₂RR)

The adsorption and subsequent activation of CO_2 following an initial reduction of the clusters exhibit significant variations depending on the presence or absence of the S atoms in the MOF clusters. Weak physisorption is observed for CO_2 on both clusters with an O-oriented binding motif (Figure 3a and 3d), and there is little to no

change in the atomic charges of the atoms of the ${\rm CO}_2$ molecules (Table 3). After adsorption, the activation of CO₂ proceeds through a single transition state where one of the C=O double bonds is broken. On the Fe₂DOBDC cluster, this transition state (Figure 3b) occurs with a barrier of 0.14 eV (3.3 kcal mol⁻¹), coinciding with an accumulation of charge of -0.18 on the CO2 adsorbate. The C atom of the transition state becomes less positively charged (from 0.42 to 0.32) while the O atoms each become more negatively charged. Activation of CO2 on Fe₂DSBDC (Figure 3e) occurs with a activation barrier of 0.74 eV (17.0 kcal mol⁻¹) which is significantly higher than on the Fe₂DOBDC cluster. This transition state results in a greater amount of charge accumulation on the CO₂ adsorbate of -0.29, possibly due to the more facile charge delocalization of the Fe₂DSBDC cluster. The low barrier for CO2 activation on the Fe2DOBDC cluster may indicate that CO2 reduction will be more readily achieved

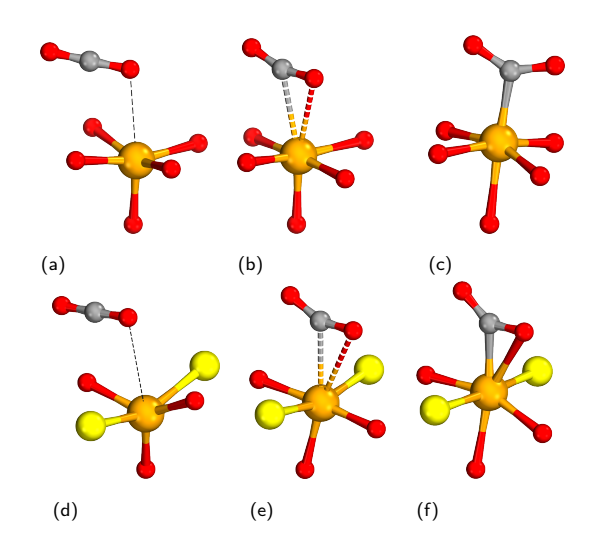


Fig. 3 Molecular structures depicting the first coordination sphere of the Fe₂DOBDC (top row) and Fe₂DSBDC (bottom row) clusters following adsorption and activation of CO₂. Physisorbed CO₂ shown to the left, the transition state is depicted in the middle, and the fully activated complex is shown to the right. Color code: C (grey), O (red), S (yellow), Fe (orange).

than on the Fe_2DSBDC cluster based on the chemical kinetics.

The initial PCET step for CO2 reduction on the neutral Fe-MOF clusters favors the formation of the *OCHO intermediate via C atom reduction over the formation of the *OCOH intermediate following O atom reduction (Figure 4). As with hydrogen reduction, we investigated the relative difference between *OCHO formation on the S and Fe sites of Fe₂DSBDC. We found a large difference of 0.92 eV, indicating more favorable reduction on the Fe sites. The difference in free energy between the formation of *OCHO and *OCOH intermediates is more significant on the Fe₂DSBDC cluster, with a value of -0.64 eV, compared to -0.33 eV on the Fe₂DOBDC cluster. This energetic preference for the *OCHO intermediate may arise from greater amount of orbital stabilization through the Fe-O bonds as opposed to the Fe-C bonds. The molecular orbitals for the *OCHO intermediates primarily consist of O p-orbitals donating electron density into the empty Fe p- and d-orbitals, while the *OCOH intermediates result in molecular orbitals that are composed of a combination of C p-orbitals and Fe d-orbitals (Figure S5). The reaction energetics for the first PCET step are remarkably close between the two clusters, with Fe₂DOBDC requiring 1.14 eV while Fe₂DSBDC requires 1.02 eV. These results resemble those observed for hydrogen reduction, indicating that some of the reduction steps proceed with similar

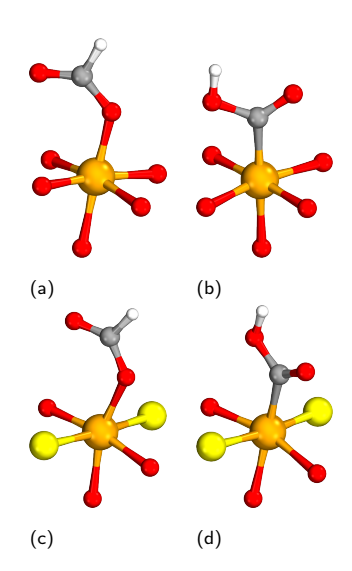


Fig. 4 Molecular structures depicting the first coordination sphere of the Fe_2DOBDC (top row) and Fe_2DSBDC (bottom row) clusters following the first PCET step to form *OCHO (left) and *OCOH (right). Color code: H (white), C (grey), O (red), S (yellow), Fe (orange).

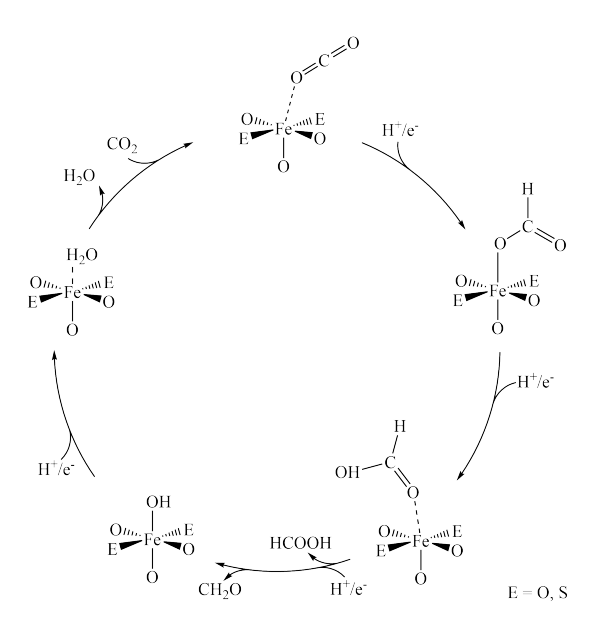


Fig. 5 Mechanistic cycle for the reduction of CO_2 to HCOOH and CH_2O . E=O or S for Fe_2DOBDC or Fe_2DSBDC , respectively.

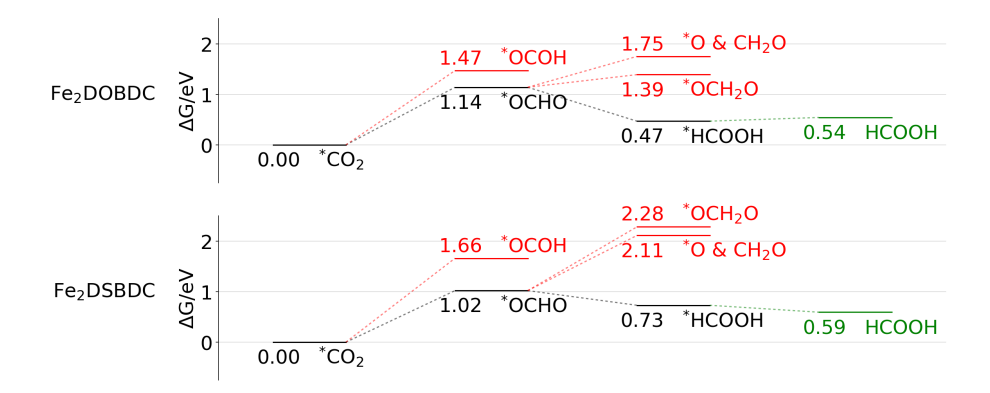


Fig. 6 Free energy profile for the reduction of CO_2 to HCOOH on the Fe_2DOBDC (top) and Fe_2DSBDC (bottom) clusters. All energy values are relative to *CO_2 for each respective cluster. Color code - favorable reduction (black), unfavorable reduction (red), desorption (green).

energetics given the different MOF clusters.

A subsequent PCET step on both clusters strongly favors the formation of *HCOOH over *OCH2O or *O & CH2O (Figures 5 & 6). This suggests that the Fe₂DOBDC and Fe₂DSBDC clusters should selectively yield HCOOH as the only 2e⁻ reduced CO₂ product, as the formation of *OCOH is highly disfavored, hindering the formation of CO. While the reduction of CO₂ proceeds similarly on the Fe₂DOBDC and Fe₂DSBDC clusters, the binding of *HCOOH to the Fe sites differs significantly. On Fe₂DOBDC, the binding of *HCOOH is favorable by -0.07 eV, indicating that *HCOOH may remain adsorbed to the site and undergo further reduction. Conversely, the Fe₂DSBDC cluster results in a *HCOOH binding energy of 0.14 eV. A positive binding energy suggests that the *HCOOH intermediate is unlikely to remain adsorbed to the surface and should instead form as the sole product of CO2 reduction. This trend may result from the less favorable van der Waals interaction due to the larger S atoms or the greater electron delocalization from the Fe-S bonds, aiding in more facile electron transport while lowering the affinity of the closed-shell adsorbates to the Fe site.

Examining subsequent PCET steps involving the adsorbed * HCOOH intermediate on the Fe₂DOBDC cluster, the most favorable intermediate to form is * OH, accompanied by the release of free CH₂O (Figure 5). This reaction step includes the reduction of the C atom and the subsequent breaking of the C-O bond. A modest input of energy (0.07 eV) compared to the first PCET step (1.14 eV) is required and ultimately leads to the formation of H₂O following an additional PCET step. Notably, the * OH intermediate exhibits strong binding to the Fe site (-2.87 eV), reducing the likelihood of further reduction of CH₂O. The

weak but favorable binding of *HCOOH to the Fe site in Fe₂DOBDC, combined with the nearly facile formation of *OH, suggests that CO₂ reduction is likely to result in the formation of both HCOOH and CH₂O on the Fe₂DOBDC MOF. This trend differs from our previous work, ¹⁵ but we believe that the different solvent environments and a more refined cluster model help stabilize the *OH intermediate, limiting further reduction to CH₄.

3.4 CO Reduction Reaction (CORR)

To gain deeper insights into the impact of S atom substitution on electrocatalytic reduction reactions within the MOF-74 framework, we extend our investigation beyond CO₂ reduction to explore the reduction of CO, potentially yielding a range of products beyond HCOOH and CH2O. The binding of CO to the Fe site is notably stronger on the Fe₂DOBDC cluster, exceeding that on Fe₂DSBDC by 0.34 eV, a trend reminiscent of what we observed with both CO₂ and HCOOH. Additionally, a more pronounced charge accumulation is observed for CO on the Fe₂DOBDC cluster (-0.17) compared to the Fe₂DSBDC (-0.12). Furthermore, upon CO adsorption to the Fe₂DOBDC cluster, the CO stretching frequency experiences a red-shift of 285.7 cm⁻¹, while the weaker binding on the Fe₂DSBDC cluster results in a smaller red-shift of 231.0 cm⁻¹. These trends underscore the distinct influence of the ligand on CO adsorption to the respective Fe-sites.

The most thermodynamically favorable pathway for CO reduction on both clusters mirrors each other. Unlike CO_2 reduction, where a pattern of alternating C and O reduction leads to the formation of either HCOOH or CH_2O , CO reduction exhibits a consistent pattern, culminating in

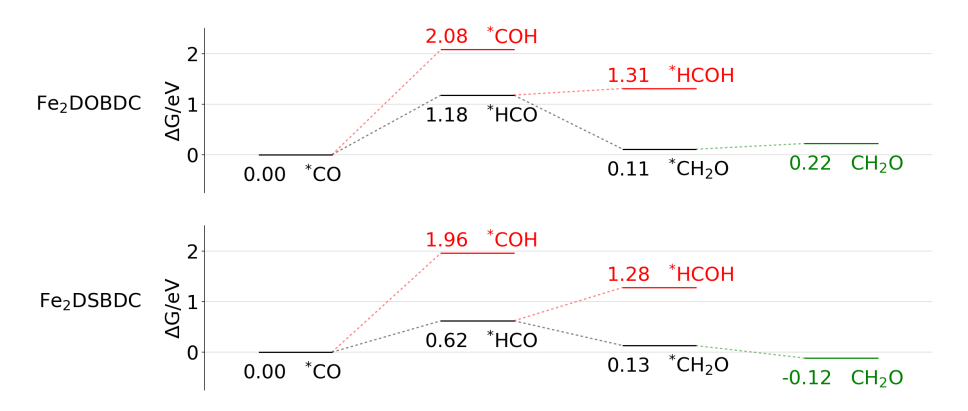


Fig. 7 Free energy profile for the reduction of CO to CH_2O on the (top) Fe_2DOBDC and (bottom) Fe_2DSBDC clusters. All energy values are relative to *CO for each respective cluster. Color code - favorable reduction (black), unfavorable reduction (red), desorption (green).

the complete reduction of the C atom to CH_4 followed by the subsequent reduction of the resulting O atom to form H_2O (Figure S6). The intermediates in this pathway include *CO , *HCO , *CH_2O , *CH_3O , *O , *OH , *H_2O .

The disparities between the Fe₂DOBDC and Fe₂DSBDC clusters results in significant differences in the energetics of CO reduction (Figures 7 & 8). The initial reduction of *CO to *HCO yields limiting potentials of 1.18 eV and 0.62 eV for Fe₂DOBDC and Fe₂DSBDC, respectively. This substantial difference in limiting potentials for CO reduction on the two clusters (0.56 eV) surpasses that observed for CO₂ reduction (0.12 eV), emphasizing the distinct electrocatalytic capabilities of these materials. Moreover, a subsequent PCET step yielding *CH2O results in significant differences in binding to the Fe sites. On Fe₂DOBDC, the *CH₂O intermediate exhibits favorable binding with a ΔG value of -0.11 eV, while the same intermediate results in unfavorable binding equal to 0.25 eV on Fe₂DSBDC. This strong desorption quality of the *CH2O intermediate on Fe₂DSBDC suggests that further reduction is improbable, indicating a high selectivity for CH₂O formation. Conversely, the Fe₂DOBDC cluster results in favorable binding for all of the reduced intermediates, ultimately leading to the favorable formation of CH₄ and H₂O following six PCET steps (Figure 8). Hence, distinct product distributions for CO reduction on Fe₂DOBDC and Fe₂DSBDC clusters are anticipated, driven by the the binding of *CH₂O to the Fe site.

4 Conclusions

Our investigation into the electrocatalytic reduction reactions on Fe-MOF-74 clusters, with and without S-substitution, has uncovered substantial behavioral differences. Earlier experimental work highlighted enhanced

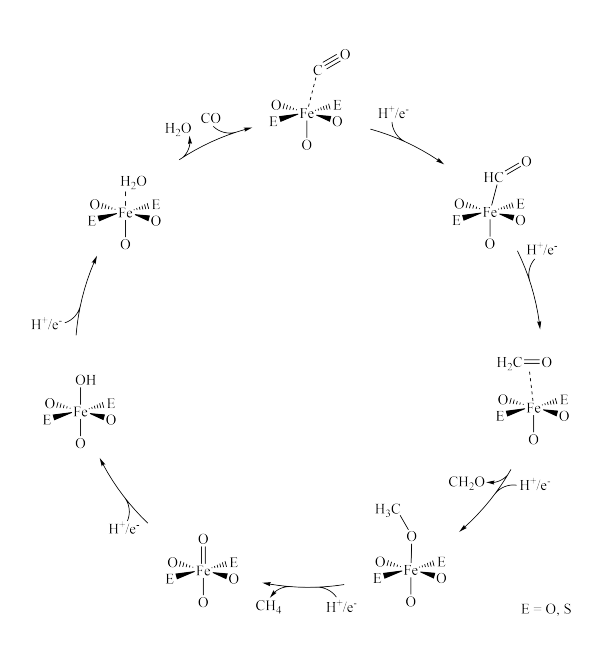


Fig. 8 Mechanistic cycle for the reduction of CO to CH_2O and CH_4 . E=O or S for Fe_2DOBDC or Fe_2DSBDC , respectively.

electrical conductance upon replacing the DOBDC ligand with DSBDC, credited to the introduction of the heavier S atoms. Despite retaining the same topological structure, the S atoms in Fe₂DSBDC induce distinct electronic structure variances compared to Fe₂DOBDC. The nature of the equatorial O atoms of Fe₂DOBDC result in stronger binding of the closed-shell reduction products, leading to the formation of deeper reduction products (CH₂O and CH₄) during CO2 and CO reduction. Conversely, the larger and less electronegative equatorial S atoms of Fe₂DSBDC lead to weakened interactions with closed-shell reduction products, yielding only 2e⁻ products (HCOOH and CH₂O). These differences do not seem to affect the reduction of hydrogen, however, which resulted in nearly identical limiting potentials between the two systems. Our findings suggest the potential for engineering other MOFs by manipulating metal-ligand interactions, offering insights into tailoring catalysts for selective electrochemical transformations.

Author Contributions

G.A.M.: conceptualization, data curation, formal analysis, investigation, methodology, software, validation, visualization, writing - original draft; T.Y. and W.Z.: project administration, resources, supervision.

42

Conflicts of interest

There are no conflicts to declare.

Acknowledgements

G.A.M would like to thank NIST's Postdoctoral Program for an NRC Postdoctoral Fellowship and Morgan Kramer for insightful discussions around this work.

Notes and references

- 1 M. Yousaf, M. Zaman, A. Mahmood, M. Imran, A. Elkamel, M. Rizwan, T. Wilberforce and F. Riaz, *Energy Science & Engineering*, 2022, 10, 4890–4923.
- 2 M. He, S. Piao, C. Huntingford, H. Xu, X. Wang, A. Bastos, J. Cui and T. Gasser, *Communications Earth & Environment*, 2022, **3**, 160.
- 3 J. S. Sperry, M. D. Venturas, H. N. Todd, A. T. Trugman, W. R. L. Anderegg, Y. Wang and X. Tai, *Proceedings of the National Academy of Sciences*, 2019, **116**, 25734–25744.
- 4 S. Nitopi, E. Bertheussen, S. B. Scott, X. Liu, A. K. Engstfeld, S. Horch, B. Seger, I. E. L. Stephens, K. Chan, C. Hahn, J. K. Nørskov, T. F. Jaramillo and I. Chorkendorff, *Chemical Reviews*, 2019, **119**, 7610–7672.

- 5 W. Ma, X. He, W. Wang, S. Xie, Q. Zhang and Y. Wang, *Chemical Society Reviews*, 2021, **50**, 12897–12914.
- 6 B. Ruqia, G. M. Tomboc, T. Kwon, J. Kundu, J. Y. Kim, K. Lee and S.-I. Choi, *Chem Catalysis*, 2022, 2, 1961– 1988.
- 7 C. Li, H. Zhang, M. Liu, F.-F. Lang, J. Pang and X.-H. Bu, *Industrial Chemistry & amp Materials*, 2023, 1, 9–38.
- 8 Q. Wang and D. Astruc, Chemical Reviews, 2019, 120, 1438–1511.
- L. S. Xie, G. Skorupskii and M. Dincă, *Chemical Reviews*, 2020, 120, 8536–8580.
- 10 R. Shah, S. Ali, F. Raziq, S. Ali, P. M. Ismail, S. Shah, R. Iqbal, X. Wu, W. He, X. Zu, A. Zada, Adnan, F. Mabood, A. Vinu, S. H. Jhung, J. Yi and L. Qiao, Coordination Chemistry Reviews, 2023, 477, 214968.
- 11 L. Sun, C. H. Hendon, M. A. Minier, A. Walsh and M. Dincă, *Journal of the American Chemical Society*, 2015, **137**, 6164–6167.
- 12 G. Fu, A. Polity, N. Volbers, B. K. Meyer, B. Mogwitz and J. Janek, *Applied Physics Letters*, 2006, **89**, year.
- 13 S. Ali, P. M. Ismail, F. Wahid, A. Kumar, M. Haneef, F. Raziq, S. Ali, M. Javed, R. U. Khan, X. Wu, H. Xiao, G. Yasin, L. Qiao and H. Xu, Fuel Processing Technology, 2022, 236, 107427.
- 14 S. Ali, P. M. Ismail, M. Humayun, M. Bououdina and L. Qiao, Fuel Processing Technology, 2024, 255, 108049.
- 15 G. A. McCarver, T. Yildirim and W. Zhou, *ChemPhysChem*, 2023, **24**, year.
- 16 K. Li and D. Xue, *The Journal of Physical Chemistry A*, 2006, **110**, 11332–11337.
- 17 R. G. Pearson, *Journal of the American Chemical Society*, 1963, **85**, 3533–3539.
- 18 K. E. Laidig and R. F. W. Bader, *The Journal of Chemical Physics*, 1990, **93**, 7213–7224.
- 19 D. J. Xiao, E. D. Bloch, J. A. Mason, W. L. Queen, M. R. Hudson, N. Planas, J. Borycz, A. L. Dzubak, P. Verma, K. Lee, F. Bonino, V. Crocellà, J. Yano, S. Bordiga, D. G. Truhlar, L. Gagliardi, C. M. Brown and J. R. Long, *Nature Chemistry*, 2014, 6, 590–595.
- 20 T. Van Phuc, S. G. Kang, J. S. Chung and S. H. Hur, *Mater. Res. Bull.*, 2021, **138**, 111228.
- 21 I. Choi, Y. E. Jung, S. J. Yoo, J. Y. Kim, H.-J. Kim, C. Y. Lee and J. H. Jang, *J. Electrochem. Sci. Technol.*, 2017, 8, 61–68.
- 22 E. E. Benson, C. P. Kubiak, A. J. Sathrum and J. M. Smieja, *Chem. Soc. Rev.*, 2009, **38**, 89–99.

- 23 G. A. McCarver, T. Rajeshkumar and K. D. Vogiatzis, *Coordination Chemistry Reviews*, 2021, **436**, 213777.
- 24 P. Verma, K. D. Vogiatzis, N. Planas, J. Borycz, D. J. Xiao, J. R. Long, L. Gagliardi and D. G. Truhlar, Journal of the American Chemical Society, 2015, 137, 5770–5781.
- 25 G. McCarver, T. Yildirim and W. Zhou, *Physical Chemistry Chemical Physics*, 2024.
- 26 Y. Zhao and D. G. Truhlar, *The Journal of Chemical Physics*, 2006, **125**, 194101.
- 27 S. Grimme, J. Antony, S. Ehrlich and H. Krieg, *The Journal of Chemical Physics*, 2010, **132**, 154104.
- 28 F. Neese, F. Wennmohs, U. Becker and C. Riplinger, *The Journal of Chemical Physics*, 2020, **152**, 224108.
- 29 F. Weigend and R. Ahlrichs, *Physical Chemistry Chemical Physics*, 2005, **7**, 3297.
- 30 J. Kalinowski, F. Wennmohs and F. Neese, *Journal of Chemical Theory and Computation*, 2017, **13**, 3160–3170.
- 31 F. Weigend, *Physical Chemistry Chemical Physics*, 2006, **8**, 1057–1065.
- 32 V. Barone and M. Cossi, *The Journal of Physical Chemistry A*, 1998, **102**, 1995–2001.

- 33 A. V. Marenich, S. V. Jerome, C. J. Cramer and D. G. Truhlar, *Journal of Chemical Theory and Computation*, 2012, **8**, 527–541.
- 34 T. Lu and F. Chen, Journal of Computational Chemistry, 2012, 33, 580–592.
- 35 J. Pipek and P. G. Mezey, *The Journal of Chemical Physics*, 1989, **90**, 4916–4926.
- 36 G. Knizia, Journal of Chemical Theory and Computation, 2013, 9, 4834–4843.
- 37 G. Knizia and J. E. M. N. Klein, *Angewandte Chemie International Edition*, 2015, **54**, 5518–5522.
- 38 S. Grimme, *Chemistry A European Journal*, 2012, **18**, 9955–9964.
- 39 R. Tyburski, T. Liu, S. D. Glover and L. Hammarström, *Journal of the American Chemical Society*, 2021, **143**, 560–576.
- 40 G.-G. Luo, H.-L. Zhang, Y.-W. Tao, Q.-Y. Wu, D. Tian and Q. Zhang, *Inorg. Chem. Front*, 2019, **6**, 343–354.
- 41 A. A. Peterson, F. Abild-Pedersen, F. Studt, J. Rossmeisl and J. K. Nørskov, *Energy and Environmental Science*, 2010, **3**, 1311–1315.
- 42 E. Boutin, L. Merakeb, B. Ma, B. Boudy, M. Wang, J. Bonin, E. Anxolabéhère-Mallart and M. Robert, Chemical Society Reviews, 2020, 49, 5772–5809.